CoFeVSb: A promising candidate for spin valve and thermoelectric applications

Jadupati Nag [1], Deepika Rani,[1,2] Durgesh Singh,[1] R. Venkatesh,[3] Bhawna Sahni,[1] A. K. Yadav [4], S. N. Jha [4], D. Bhattacharyya,[4] P. D. Babu,[5] K. G. Suresh,[1,*] and Aftab Alam [1,†]

[1]*Department of Physics, Indian Institute of Technology Bombay, Mumbai 400076, India*
[2]*Department of Physics, Indian Institute of Technology Delhi, New Delhi 110016, India*
[3]*UGC-DAE Consortium for Scientific Research, University Campus, Khandwa Road, Indore 452001, India*
[4]*Atomic & Molecular Physics Division, Bhabha Atomic Research Centre, Mumbai 400094, India*
[5]*UGC-DAE Consortium for Scientific Research, Mumbai Centre, BARC Campus, Mumbai 400085, India*

We report a combined theoretical and experimental study of a novel quaternary Heusler system, CoFeVSb, from the viewpoint of room-temperature spintronics and thermoelectric applications. CoFeVSb crystallizes in a cubic structure with a small DO_3-type disorder. The presence of the disorder is confirmed by room-temperature synchrotron x-ray diffraction and extended x-ray absorption fine structure measurements. Magnetization data reveal a high ordering temperature ($\sim$850 K) with a saturation magnetization of 2.2 μ_B/f.u. Resistivity measurements indicate a half-metallic or semimetallic nature. A double hysteresis loop along with asymmetry in the magnetoresistance data reveals a room-temperature spin valve feature, which remains stable even at 300 K. Hall measurements show anomalous behavior with a significant contribution from the intrinsic Berry phase. This alloy also has a large room-temperature power factor ($\sim$0.62 mW m^{-1} K^{-2}) and ultralow simulated lattice thermal conductivity ($\sim$0.4 W m^{-1} K^{-1}), making it a promising candidate for thermoelectric application. *Ab initio* calculations suggest weak spin-polarized semimetallic behavior and reduced magnetization (in agreement with the experiment) in the presence of DO_3 disorder. We have also found an energetically competing ferromagnetic (FM)/antiferromagnetic interface structure within an otherwise FM matrix, one of the prerequisites for spin valve behavior. The coexistence of so many promising features in a single system is rare, and hence CoFeVSb gives a fertile platform to explore numerous applications in the future.

I. INTRODUCTION

Heusler alloys have drawn enormous attention in several fields due to their interesting properties. Most of them are versatile and quite promising because of their robust structure, high Curie temperature T_C, and high spin polarization; hence they are highly suited for spin-transport applications. Half-metallic ferromagnets (HMFs) [1,2], which are one of the earliest classes of spin-polarized materials, have led to a revolution in the field of spintronics. HMFs possess a unique electronic structure exhibiting a finite band gap in one spin channel and metallic behavior in the other. There are a large number of materials in the Heusler family [3–6] which are reported to be HMFs and are predicted to show 100% spin polarization because of the complete absence of minority spin states at the Fermi level (E_F). Such materials are in great demand for applications such as magnetic tunnel junctions [7,8], spin injectors, spin valves [9,10], etc. A spin valve is a device, consisting of two or more conducting magnetic layers, where electrical resistance can change between two values depending on the relative alignment of the magnetization in the layers. The resistive state of such a composite system can

be switched by changing the direction of the applied magnetic field, resulting in asymmetric magnetoresistance (MR). The spin valve concept is often used in devices such as magnetic sensing, recording, etc. This feature is generally observed in multilayer ferromagnetic thin films [11] and is extremely rare in bulk materials [12]. Another important research area in which Heusler alloys, especially half-Heusler alloys, are found promising is thermoelectric (TE) applications [13–15].

In this paper, we report a combined theoretical and experimental study of the promising spin valve and TE properties of a quaternary Heusler alloy, CoFeVSb (CFVS). Though there exists a theoretical study of ordered CFVS [16] predicting its half-metallic behavior, our study fills the need for an experimental and theoretical investigation reporting its potential for spin valve and TE applications. Using combined synchrotron x-ray diffraction (XRD) and x-ray absorption fine structure (EXAFS) measurements, we confirm CFVS to crystallize in a LiMgPdSn structure with robust partial DO_3 disorder. Our *ab initio* calculations confirm the half-metallic nature of CFVS in its ordered phase, as reported earlier. The disordered DO_3 structure, however, makes it a weakly spin-polarized semimetal, as also supported by our transport measurement. The measured saturation magnetization is found to be 2.2 μ_B/f.u. along with a high T_C ($\sim$850 K), in fair agreement with theory. Magnetization and MR data strongly indicate room-temperature (RT) spin valve features in this alloy. A

*suresh@phy.iitb.ac.in
†aftab@phy.iitb.ac.in

careful analysis of Hall data indicates the dominance of the intrinsic Berry phase contribution to the anomalous Hall effect (AHE). CFVS also shows promise for TE applications, with a high thermopower (~ 0.62 mW m^{-1} K^{-2}) and ultralow simulated lattice thermal conductivity (~ 0.4 W m^{-1} K^{-1}) at RT. The high T_C, robust structure, spin-polarized semimetallic nature, promising spin valve, and thermoelectric properties make CFVS a potential candidate for multifunctional applications.

II. EXPERIMENTAL AND COMPUTATIONAL DETAILS

A. Experimental details

Polycrystalline samples of CoFeVSb were synthesized using an arc-melting system in a high-purity Ar environment of the stoichiometric quantities of the constituent elements having a purity of at least 99.99% (to compensate for the losses during melting, we have taken 1.5% extra Sb with respect to the stoichiometric amount). To stabilize the desired phase, samples were annealed for 1 week at 900 °C in sealed quartz tubes, followed by quenching in ice water. For the structural studies, XRD patterns at RT were taken using Cu-Kα radiation with the help of a Panalytical X'Pert diffractometer. Crystal structure analysis was done using FULLPROF SUITE software [17]. EXAFS measurements were carried out at the Energy-Scanning EXAFS beamline (BL-9) in transmission mode at the INDUS-2 Synchrotron Source (2.5 GeV, 200 mA) at the Raja Ramanna Centre for Advanced Technology (RRCAT), Indore, India [18,19]. Elemental analysis of the alloy was performed at an environmental scanning electron microscope (ESEM) facility (FEI, Quanta 200). The detailed results of the energy-dispersive spectra (EDS) are shown in the compositional analysis section of the Supplemental Material (SM) [20]. Magnetization measurements at various temperatures were obtained using a vibrating sample magnetometer (VSM) attached to a physical property measurement system (PPMS; Quantum Design) for fields up to 70 kOe. Temperature- and field-dependent resistivity measurements were carried out using a PPMS (DynaCool) employing the electrical transport option (ETO) in the four-probe method (10 mA current at 18 Hz frequency). Hall measurements were also carried out using the same setup, with the van der Pauw method under the same current and frequency. Thermoelectric power (TEP) was measured using the differential dc sandwich method in an in-house setup in the temperature range of 4–300 K [21]. For the EXAFS measurements, the Energy-Scanning EXAFS beamline (BL-9) was operated in the energy range of 4–25 keV. The beamline optics consisted of a Rh/Pt-coated collimating meridional cylindrical mirror, and the collimated beam reflected by the mirror was monochromatized by a Si(111) ($2d = 6.2709$ Å) based double crystal monochromator (DCM). The second crystal of the DCM was a sagittal cylinder, which was used for horizontal focusing while a Rh/Pt-coated bendable post mirror facing down was used for vertical focusing of the beam at the sample position. Three ionization chambers (300 mm length each) were used for data collection in transmission mode, one ionization chamber for measuring incident flux I_0, the second for measuring transmitted flux I_T, and the third for measuring the

EXAFS spectrum of a reference metal foil for energy calibration. The appropriate gas pressure and gas mixture were chosen to achieve 10–20% absorption in the first ionization chamber and 70–90% absorption in the second ionization chamber to improve the signal-to-noise ratio. Rejection of the higher harmonics content in the x-ray beam was performed by a second mirror. The absorption coefficient was obtained using the relation $I_T = I_0 e^{-\mu x}$. Synchrotron XRD measurements were carried out using the synchrotron wavelength $\lambda = 0.6525$ Å. Synchrotron-based powder x-ray diffraction measurements were performed on well-ground powder samples at the extreme conditions angle dispersive/energy dispersive x-ray diffraction (EC-AD/ED-XRD) beamline (BL-11) at the Indus-2 synchrotron source. Measurements were carried out in capillary mode, and the capillary was rotated at ~ 150 rpm to reduce the orientation effects. The desired wavelength for ADXRD experiments was selected from the white light from the bending magnet using a Si(111) channel-cut monochromator. The monochromatic beam was then focused onto the sample with a Kirkpatrick-Baez mirror, or K-B mirror. A MAR345 image plate detector (which is an area detector) was used to collect two-dimensional (2D) diffraction data. The sample-to-detector distance and the wavelength of the beam were calibrated using the National Institute of Standards and Technology (NIST) standards LaB$_6$ and CeO$_2$. Calibration and conversion-integration of 2D diffraction data to 1D, intensity vs 2θ, were carried out using FIT2D software [22]. The surface morphology of the bulk sample was analyzed by atomic force microscopy (AFM) and magnetic force microscopy (MFM) using a NanoScope Multimode-IV (Veeco, Digital Instruments). Transmission electron microscopy (TEM) images and selected area electron diffraction (SAED) patterns were recorded using a field emission gun TEM (FEG-TEM; Philips CM200) on a powder sample.

B. Computational details

Ab initio calculations were performed using spin-polarized density functional theory (DFT) [23] implemented within the Vienna *ab initio* simulation package (VASP) [24–26] with a projected augmented-wave (PAW) basis [27]. The exchange-correlation potential due to Perdew, Burke, and Ernzerhof (PBE) [28] was used within the generalized gradient approximation (GGA) scheme. Brillouin zone integration was done within the tetrahedron method using a $24 \times 24 \times 24$ k mesh. A plane-wave energy cutoff of 500 eV was used for all the calculations. All the structures were fully relaxed with total energies (forces) converged to values less than 10^{-6} eV (0.01 eV/Å). In order to further evaluate the potential of CFVS for thermoelectric (TE) applications, we simulated the lattice thermal conductivity κ_L using the *Ab Initio* Conductivities (AICON) code [29]. AICON is the modified Debye-Callaway (DC) model, which calculates κ_L by including the contribution from both acoustic and optical phonon branches scaled by their specific heat ratio. The mode velocities, Debye temperature, and mode Grüneisen parameters are some of the key quantities used as the input parameters for this model and were calculated from the phonon band structure using the PHONOPY code [30]. This requires density functional
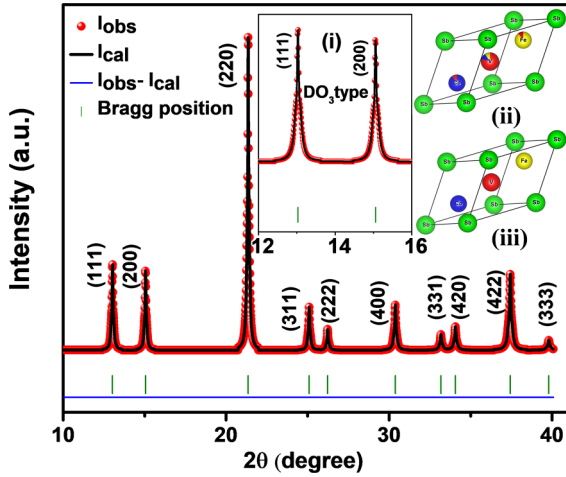
FIG. 1. For CoFeVSb, synchrotron XRD pattern at RT including the Rietveld refined data for the type-I configuration with partial DO$_3$ disorder. Inset (i) shows a zoomed-in view near the (111) and (200) peaks. Insets (ii) and (iii) display the crystal structures for partial DO$_3$ disorder and pure Y type.
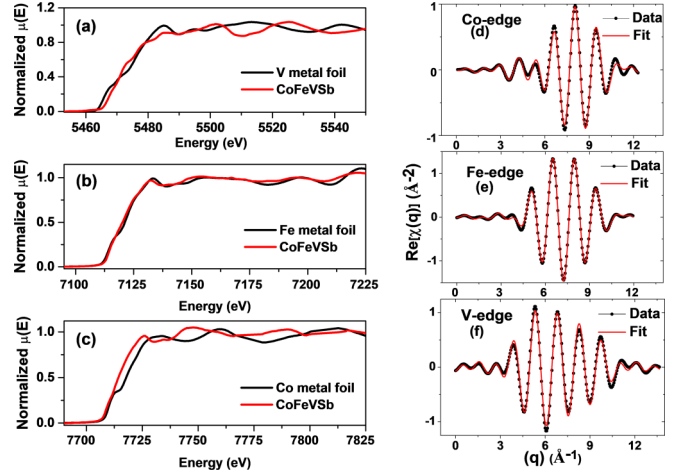

FIG. 2. For CoFeVSb, normalized XANES spectra at the (a) V K edge, (b) Fe K edge, and (c) Co K edge along with that of the corresponding metal foil. (d), (e), and (f) Inverse Fourier transformed EXAFS spectra at the Co, Fe, and V K edges, respectively (points), along with the theoretical fit (solid red line).

perturbation theory (DFPT) [31] calculations, as implemented within VASP [24–26]. The mode velocities v for acoustic modes are calculated by taking the slope of the band corresponding to the vibrational mode at the Γ point. The Debye temperature θ is obtained from the maximum frequency corresponding to the vibrational mode. In addition to v and θ, this model for the lattice thermal conductivity also requires the mode Grüneisen parameters γ_i. γ is a measure of the degree of anharmonicity of the lattice. The higher the γ value, the more anharmonic the lattice will be. κ_L is defined as

$$\kappa_L = R_A \frac{\kappa_{LA} + \kappa_{TA} + \kappa_{TA'}}{3} + R_O \kappa_O, \qquad (1)$$

where LA denotes longitudinal acoustic, TA/TA' denote two transverse acoustic branches, and O denotes the optical phonon branches. $R_A = c_V^{aco}/(c_V^{aco} + c_V^{opt})$ and $R_O = c_V^{opt}/(c_V^{aco} + c_V^{opt})$ are the specific heat ratios for acoustic and optical branches, respectively, and c_V^i are the specific heat of the respective phonon branches (i = acoustic or optical).

III. RESULTS AND DISCUSSION

A. Experimental results

1. Crystal structure (x-ray diffraction)

CFVS crystallizes in the LiMgPdSn prototype structure (space group $F\bar{4}3m$) with lattice parameter 5.82 Å. There exist three nondegenerate crystal configurations for any equiatomic quaternary Heusler structure [32]. These are discussed in Sec. III B, which confirms type I to be the energetically most stable configuration. Figure 1 shows the Rietveld refined (χ^2 = 0.5) synchrotron XRD (SXRD) pattern (using $\lambda = 0.6525$ Å) at RT, where the type-I configuration with 12.5% disorder between Co and V (X and Y) atoms and 12.5% disorder between Fe and V (X′ and Y) atoms is considered for fitting. This combination gives the best fitting compared with all the other ordered and disordered ones we tried. Normal XRD data show a similar trend for Rietveld refinement; see SM [20].

Inset (i) of Fig. 1 shows a zoomed-in view of the refined SXRD data near the (111) and (200) peaks. As these superlattice reflections are very prominent, the possibility of A2- or B2-type disorder is ruled out. There may be some possibility of DO$_3$ disorder because of a slight reduction in the (200) peak intensity in comparison to the (111) peak. This is also predicted by our EXAFS data, described below. In general, for an XX′YZ alloy, intermixing of X or X′ with Y sites or intermixing of X or X′ with Z sites yields DO$_3$-type disorder. In the present case, we have considered only the swap disorder involving X or X′ and Y (Co or Fe with V) since EXAFS measurements have not found any contribution from swapping of Sb with Co or Fe. Insets (ii) and (iii) display the crystal structures for partial DO$_3$ disorder and pure Y type.

2. Crystal structure (EXAFS)

Figure 2 shows the x-ray absorption near-edge structure (XANES) spectra of CFVS at Co, Fe, and V K edges along with those of the respective metal foils. These K edges coincide with the edges of their respective metal foils, indicating the absence of oxide phases. The oscillations in the spectra immediately above the absorption edge are completely different as compared with their respective foils for Co and V K edges. The variation of the absorption profile for three different edges arises because the XANES spectrum (immediate energy range of the absorption edge) profile not only depends on the local coordination geometry but also depends on bond distances. The q^2 weighted $\chi(q)$ vs q spectra are shown in Figs. 2(d)–2(f).

The $\chi(q)$ vs q spectra [generated from the inverse Fourier transform of $k^2\chi(R)$] are shown in Figs. 2(d)–2(f) measured at the Co, Fe, and V K edges. Figures 2(d)–2(f) show the best-fit $\chi(q)$ vs q spectra, along with the experimental data. The antisite disorder paths have been generated by swapping the absorption atom site. The bond distances, the disorder (Debye-Waller) factor σ^2 which gives the mean-square fluctuations in the distances, and the fraction of antisite disorder
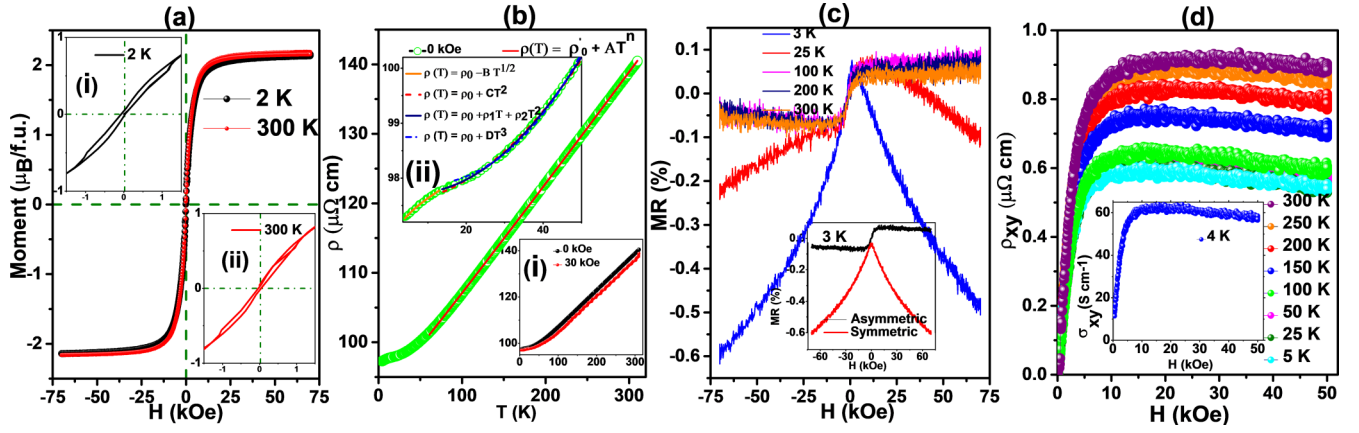
FIG. 3. For CoFeVSb, (a) M vs H curves at 2 and 300 K. Insets (i) and (ii) display zoomed-in views. (b) Longitudinal resistivity ρ vs T, along with the power-law fitting in the high-T range. Inset (i) shows ρ vs T at 0 and 30 kOe fields, while inset (ii) shows a zoomed-in view of the low-T behavior, along with various fitting models. (c) MR vs H at various T. The inset shows the asymmetric and symmetric components at 3 K. (d) Hall resistivity ρ_{xy} vs H at different T. The inset shows the Hall conductivity vs H at 4 K.

x are used as the fitting parameters (given in Table S1 of the SM [20]). The Fourier transforms of the EXAFS spectra at the V, Fe, and Co K edges along with theoretical fit are shown in Fig. S6 of the SM [20]. The first coordination peak is used for fitting because of the relatively low data range $k = 3$–10 Å^{-1}. From the fitting, it appears that there is no contribution of antisite disorder due to the swapping of Sb with Co and Fe; rather it arises due to the swapping of V with Fe and Co. However, the absorption edge profile of CFVS and Fe foil is similar at the Fe K edge. The relatively smaller (2.47 Å) Fe-Fe or Fe-Co bond distance is due to the possible presence of metallic Fe, which corroborates the XANES result. Thus EXAFS measurements confirm the possibility of antisite disorder between the Co-V and Fe-V sites, giving rise to the DO$_3$ disorder, which is also supported by the XRD data.

3. Magnetic properties

Figure 3(a) shows the magnetic moment M vs magnetizing field H curves for CFVS. Insets (i) and (ii) show a zoomed-in view at 2 and 300 K. The M vs temperature T curve along with high-T magnetization data is shown in Fig. S7 of the SM [20], which indicates high T_C ($\sim$850 K) for this alloy. M-H curves show a small but nonzero hysteresis and 70-Oe coercivity (at 3 K), indicating CFVS to be a soft ferromagnet. The low-field part of the M-H curve shown in the insets clearly indicates the presence of a double hysteresis loop, a property usually signifying the spin valve effect [33]. One can also notice a steplike feature at about 1 kOe, indicating the presence of an additional, low-magnetization phase. One should also note that the total magnetic moment at 300 K is slightly higher than that at 2 K, which again indicates the possibility of small ferrimagnetic or AFM regimes. The total moment m per formula unit for a Heusler alloy can be calculated in terms of the number of valence electrons N_v [4], using the Slater-Pauling (SP) rule: $m = (N_v - 24)\,\mu_B$/f.u. [34,35]. As such, for CFVS, a moment of 3.0 μ_B/f.u. is expected in its completely ordered state. The measured moment turns out to be 2.2 μ_B/f.u. This difference is attributed partially to the antisite (DO$_3$) disorder [36] or the presence of competing magnetic ordering. This is

also supported by significant contrast in our magnetic force microscopy (MFM) data highlighting boundaries between domains of two competing magnetic phases even at RT (see Fig. S3 of the SM [20]). All these coexisting features, such as the double hysteresis loop, reduced magnetization, metamagneticlike step in the M-H loop, and contrasting regions in the MFM data, indicate the existence of some disordered phase involving FM/AFM clusters within a FM matrix. Such features are observed rarely in bulk materials and are responsible for the spin valve effect.

4. Transport properties (resistivity)

Figure 3(b) shows the temperature dependence of longitudinal resistivity ρ_{xx} at different fields (0 and 30 kOe) [see inset (i)]. ρ_{xx} increases and varies almost linearly with T towards 300 K. To get a better understanding of the variation of resistivity with T, we analyzed the data in three different T ranges: range I, $3 < T < 13$ K; range II, $14 < T < 60$ K; and range III, $60 < T < 310$ K. The details of the fitting considering different models are given in Table S2 of the SM [20]. From the fitting, it appears that the T^2 dependence is very weak, and linear behavior dominates throughout the T range (especially high T). Such a dependence at low temperatures rules out the single magnon scattering, an indication of the half-metallic nature of the alloy [3].

5. Transport properties (magnetoresistance)

Figure 3(c) shows the field dependence of MR, defined as $\mathrm{MR}(H) = [\rho(H) - \rho(0)]/\rho(0)$, at various T. The magnitude of MR is low, but it increases with H in a sublinear fashion and does not saturate till 70 kOe at 3 K. Interestingly, it shows an asymmetric feature between positive and negative fields. The inset of Fig. 3(c) shows the asymmetric and symmetric components of MR at 3 K [37]. The symmetric part is negative and shows a linear variation with H. As T is raised to 25 K, in addition to the asymmetry, one can notice a clear hump as H changes from negative to positive. At 25 K, a sharp plateaulike feature is observed at lower H, which gets suppressed at higher H giving rise to the asymmetric nature. MR exhibits
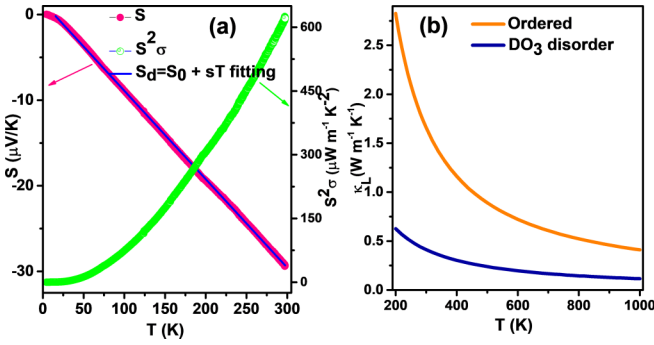
FIG. 4. For CoFeVSb, (a) Seebeck coefficient S and power factor $S^2\sigma$ vs T. The fitting to the S vs T curve illustrates the linear behavior of the diffusion thermopower ($S_d = S_0 + sT$) between 20 and 300 K. (b) Simulated lattice thermal conductivity κ_L for ordered and DO$_3$ disordered structure.

TABLE I. Relaxed lattice parameters a_0, atom projected and total magnetic moments (in μ_B), and relative energies ΔE of type-I, type-II, and type-III configurations of CoFeVSb, calculated within the GGA.

Type	a_0 (Å)	m^{Co}	m^{Fe}	m^V	m^{total}	ΔE (eV/f.u.)
I	59	1.04	1.13	0.84	3.0	0.0
II	61	1.2	1.9	−1.3	1.78	0.7
III	60	1.06	2.6	−1.11	2.55	0.36

a crossover behavior (from negative to positive) starting from 50 K, which continues till 300 K. These features of MR clearly reflect the spin-valve-like behavior [12], which remains intact in the T range of 50–300 K and even under a field of 70 kOe [38]. One should note that the double hysteresis loop also points towards the spin-valve-like feature in this alloy. The emergence of competing magnetic phases necessary for the spin valve effect is discussed in Sec. III B.

6. Transport properties (Hall measurements)

Figure 3(d) shows the Hall resistivity ρ_{xy} vs H, at different T. The H dependence of Hall conductivity ($\sigma_{xy} \approx \frac{\rho_{xy}}{\rho_{xx}^2}$) is shown in the inset. The residual σ_{xy0} is found to be 64.4 S/cm at 4 K, which is much smaller compared with that of half-metallic systems [3]. ρ_{xy} mainly consists of two contributions, (i) the ordinary Hall effect (OHE) and (ii) the anomalous Hall effect. The latter arises due to the magnetic contribution as a result of the asymmetric scattering of conducting electrons.

In general, the Hall resistivity can be expressed as [39] $\rho_{xy}(T) = \rho_{xy}^{OHE} + \rho_{xy}^{AHE} = R_0 H + R_A M$, where ρ_{xy}^{AHE}, R_0, R_A, and M are the anomalous Hall resistivity, ordinary Hall coefficient, anomalous Hall coefficient, and magnetization, respectively. In the low H range, AHE dominates, while OHE is dominant at relatively higher H. AHE contributions to ρ_{xy} can be obtained by extrapolating the high-field data to zero field. Further details of the AHE analysis are given in Sec. I(F) of the SM [20]. The negative slope of the ordinary Hall coefficient suggests electrons to be the majority charge carriers, an inference that matches with the TE results, shown below. From the fitting of the Hall data and the detailed AHE analysis (see Sec. I(F) of the SM [20]; see also Refs. [40–44] therein) we obtain a nonzero Karplus-Luttinger term, confirming a finite contribution of the intrinsic mechanism. This, in turn, indicates the dominance of the intrinsic Berry phase contribution to the AHE [45].

7. Thermoelectric properties

Figure 4(a) shows the variations of the Seebeck coefficient S and power factor $S^2\sigma$ with T. S increases linearly with T throughout the T range, which is a typical behavior of a semimetal or weak half metal. The negative slope of the S

vs T plot corresponds to a purely electron-driven S, which is reflected in the Hall data as well. The linear behavior of S suggests the dominance of diffusion thermopower. The magnitude of S is 30 μV/K at 300 K, which is fairly high and comparable to that of other potential TE materials, at RT [46–48]. The power factor shows an almost quadratic nature with a maximum value of 621 μW m^{-1} K^{-2} at RT. This is one of the highest among many Heusler-based TE materials [15] and is also in line with other reported promising TE materials [13,14,49,50]. The carrier concentration n is evaluated by fitting the S data with the equation $S_d = S_0 + sT$ in the T range of 25–300 K, where S_d is the diffusion thermopower and S_0 is a constant. $s = \frac{\pi^2 k_B^2}{eE_F}$ yields a carrier concentration of $n \simeq 10^{21}$. Typical n for promising TE materials lie in the range 10^{19}–10^{21} cm^{-3}.

To further evaluate the potential of CFVS for TE applications, we have simulated the lattice thermal conductivity κ_L with and without DO$_3$ disorder, as shown in Fig. 4(b). CFVS with DO$_3$ disorder (the actual experimental phase) shows ultralow κ_L values (0.1–0.6 W m^{-1} K^{-1}) due to the increased phonon scattering in comparison to the completely ordered phase (the phonon dispersion for both ordered and disordered phases S1 is shown in Fig. S10 of the SM [20]). Similar κ_L values are reported in a few other promising TE materials as well [51,52]. This again confirms the potential of CFVS for TE applications.

B. Theoretical results

The crystal structure of CoFeVSb can be seen as four interpenetrating fcc sublattices with Wyckoff positions 4a, 4b, 4c, and 4d. In general, for a quaternary XX′YZ alloy, there exist three energetically nondegenerate structural configurations (keeping the Z atom at the 4a site). They are as follows: (a) X at the 4c site, X′ at the 4d site, and Y at the 4b site (type I); (b) X at the 4b site, X′ at the 4d site, and Y at the 4c site (type II); and (c) X at the 4c site, X′ at the 4b site, and Y at the 4d site (type III).

Ab initio total-energy calculations are performed considering the above three different configurations for CFVS. We also simulated various magnetic states by considering different magnetic arrangements (antiferro-, ferro-, and ferrimagnetic) in all the three configurations. Table I shows the energetics, optimized lattice parameters, and moments of the most stable magnetic states of three ordered configurations. Type I turns out to be energetically the most stable configuration with ferromagnetic ordering. Figure 5(a) displays the spin-polarized band structure and density of states (DoS) for this
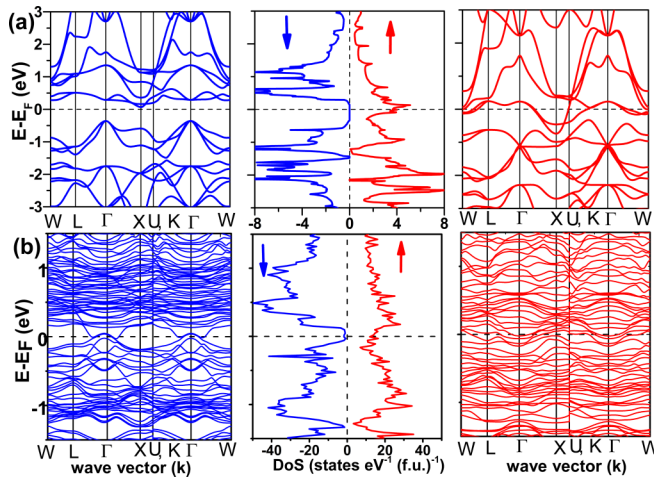
FIG. 5. Spin-polarized band structure and density of states of the type-I configuration (a) for pure Y type and (b) considering partial DO_3 disorder for CoFeVSb at $a_0 = 5.9$ Å.

configuration, which clearly shows a half-metallic nature with a band gap of 0.48 eV in the minority spin channel.

The total magnetic moment of the type-I configuration is $3.0 \, \mu_B/$f.u., which agrees well with the SP rule. In contrast, the experimentally observed moment is $2.2 \, \mu_B/$f.u. This difference is partially due to the DO_3 disorder in this system, as observed experimentally. To understand this discrepancy, we have constructed a DO_3 disordered structure of CFVS by swapping one Co atom with one V atom and one Fe atom with one V atom in a $2 \times 2 \times 2$ supercell, which gives a 12.5% swap disorder, as predicted by XRD and EXAFS measurements. See Ref. [53] for more details about this structure. The simulation of this structure indeed gives a reduced magnetization of $2.5 \, \mu_B/$f.u., in line with experimental prediction. With DO_3 disorder, the V atoms which replace Co and Fe sites remain FM but gain moment as compared with their own designated Wyckoff sites. In contrast, Co and Fe atoms which replace V sites become antiferromagnetically aligned and hence cause an overall reduction in the net moment. Also, with DO_3 disorder, CFVS becomes a weakly spin-polarized semimetal [see Fig. 5(b)], as both electron and hole carriers are seen at E_F for the spin-up band, while the spin-down band has a nearly zero gap. This is consistent with some of the observations made from the transport measurements.

Taking a hint from the spin alignment of different atoms in the DO_3 disordered structure, we have modeled a FM/AFM interface structure involving Co, Fe, and V atoms. This magnetic structure is shown in Fig. S9 of the SM [20], which clearly resembles a FM/AFM interface embedded within a host of FM matrix, supporting the spin valve behavior in CFVS. This magnetic structure is energetically close to (within 2 meV of) the lowest-energy type-I FM structure and has a net moment of $2.3 \, \mu_B/$f.u.

IV. SUMMARY AND CONCLUSION

Here, we report a new quantum material, CoFeVSb, which is predicted to be a potential candidate for spintronics and thermoelectric applications. Using a combined theoretical and experimental study, we predict CoFeVSb to host various interesting multifunctional properties such as a room-temperature spin valve nature, large power factor, high spin polarization, and extremely high T_C ($\sim$850 K). The system crystallizes in a cubic structure with a small amount of DO_3 disorder, as confirmed by both normal or synchrotron XRD and EX-AFS measurements. Electronic structure calculations with DO_3 disorder reveal CFVS to be a weakly spin-polarized semimetal. The observation of a double hysteresis loop, asymmetric magnetoresistance, and stability of the FM/AFM interface from *ab initio* calculations strongly suggests room-temperature spin valve behavior. Hall measurements show anomalous behavior, dominated by the intrinsic Berry phase contribution. Furthermore, the large power factor and ultralow simulated lattice thermal conductivity confirm CFVS to be a potential candidate for TE applications as well. In conclusion, the coexistence of many interesting properties in a single material opens up new opportunities for numerous applications such as spin calorics, thermoelectrics, etc.

[1] R. A. de Groot, F. M. Mueller, P. G. van Engen, and K. H. J. Buschow, Phys. Rev. Lett. **50**, 2024 (1983).

[2] W. E. Pickett and J. S. Moodera, Phys. Today **54**(5), 39 (2001).

[3] D. Bombor, C. G. F. Blum, O. Volkonskiy, S. Rodan, S. Wurmehl, C. Hess, and B. Büchner, Phys. Rev. Lett. **110**, 066601 (2013).

[4] T. Graf, C. Felser, and S. S. Parkin, Prog. Solid State Chem. **39**, 1 (2011).

[5] D. Rani, Enamullah, K. G. Suresh, A. K. Yadav, S. N. Jha, D. Bhattacharyya, M. R. Varma, and A. Alam, Phys. Rev. B **96**, 184404 (2017).

[6] J. Moodera and D. Mootoo, J. Appl. Phys. (Melville, NY) **76**, 6101 (1994).

[7] N. Tezuka, N. Ikeda, A. Miyazaki, S. Sugimoto, M. Kikuchi, and K. Inomata, Appl. Phys. Lett. **89**, 112514 (2006).

[8] Y. Sakuraba, N. Hirose, M. Oogane, T. Nakamura, Y. Ando, and K. Takanashi, Appl. Phys. Lett. **96**, 092511 (2010).

[9] K. Kasahara, Y. Fujita, S. Yamada, K. Sawano, M. Miyao, and K. Hamaya, Appl. Phys. Express **7**, 033002 (2014).

[10] T. Furubayashi, T. Nakatani, H. Goripati, H. Sukegawa, Y. Takahashi, K. Inomata, and K. Hono, J. Appl. Phys. (Melville, NY) **114**, 123910 (2013).

[11] B. Dieny, V. S. Speriosu, S. S. P. Parkin, B. A. Gurney, D. R. Wilhoit, and D. Mauri, Phys. Rev. B **43**, 1297 (1991).

[12] S. Singh, R. Rawat, S. E. Muthu, S. W. D'Souza, E. Suard, A. Senyshyn, S. Banik, P. Rajput, S. Bhardwaj, A. M. Awasthi, R. Ranjan, S. Arumugam, D. L. Schlagel, T. A. Lograsso, A. Chakrabarti, and S. R. Barman, Phys. Rev. Lett. **109**, 246601 (2012).

[13] B. Hinterleitner, I. Knapp, M. Poneder, Y. Shi, H. Müller, G. Eguchi, C. Eisenmenger-Sittner, M. Stöger-Pollach, Y. Kakefuda, N. Kawamoto, Q. Guo, T. Baba, T. Mori, S. Ullah, X.-Q. Chen, and E. Bauer, Nature (London) **576**, 85 (2019).

[14] F. Garmroudi, A. Riss, M. Parzer, N. Reumann, H. Müller, E. Bauer, S. Khmelevskyi, R. Podloucky, T. Mori, K. Tobita, Y. Katsura, and K. Kimura, Phys. Rev. B **103**, 085202 (2021).

[15] X. Yan, G. Joshi, W. Liu, Y. Lan, H. Wang, S. Lee, J. Simonson, S. Poon, T. Tritt, G. Chen, and Z. F. Ren, Nano Lett. **11**, 556 (2011).

[16] L. Xiong, L. Yi, and G. Gao, J. Magn. Magn. Mater. **360**, 98 (2014).

[17] J. Rodríguez-Carvajal, Phys. B: Condens. Matter **192**, 55 (1993).

[18] A. Poswal, A. Agrawal, A. Yadav, C. Nayak, S. Basu, S. Kane, C. Garg, D. Bhattachryya, S. Jha, and N. Sahoo, in Solid State Physics: *Proceedings of the 58th DAE Solid State Physics Symposium 2013*, AIP Conference Proceedings Vol. 1591 (American Institute of Physics, College Park, MD, 2014), pp. 649–651.

[19] S. Basu, C. Nayak, A. Yadav, A. Agrawal, A. Poswal, D. Bhattacharyya, S. Jha, and N. Sahoo, J. Phys. Conf. Ser. **493**, 012032 (2014).

[20] See Supplemental Material at http://link.aps.org/supplemental/10.1103/PhysRevB.105.144409 for details.

[21] L. Sharath Chandra, A. Lakhani, D. Jain, S. Pandya, P. Vishwakarma, M. Gangrade, and V. Ganesan, Rev. Sci. Instrum. **79**, 103907 (2008).

[22] A. Hammersley, S. Svensson, M. Hanfland, A. Fitch, and D. Hausermann, Int. J. High Pressure Res. **14**, 235 (1996).

[23] P. Hohenberg and W. Kohn, Phys. Rev. **136**, B864 (1964).

[24] G. Kresse and J. Furthmüller, Phys. Rev. B **54**, 11169 (1996).

[25] G. Kresse and J. Furthmüller, Comput. Mater. Sci **6**, 15 (1996).

[26] G. Kresse and J. Hafner, Phys. Rev. B **47**, 558 (1993).

[27] G. Kresse and D. Joubert, Phys. Rev. B **59**, 1758 (1999).

[28] J. P. Perdew, K. Burke, and M. Ernzerhof, Phys. Rev. Lett. **77**, 3865 (1996).

[29] T. Fan and A. R. Oganov, Comput. Phys. Commun. **251**, 107074 (2020).

[30] A. Togo and I. Tanaka, Scr. Mater. **108**, 1 (2015).

[31] S. Baroni, S. De Gironcoli, A. Dal Corso, and P. Giannozzi, Rev. Mod. Phys. **73**, 515 (2001).

[32] J. Nag, D. Rani, J. Kangsabanik, D. Singh, R. Venkatesh, P. D. Babu, K. G. Suresh, and A. Alam, Phys. Rev. B **104**, 134406 (2021).

[33] M. Yoneda, S. Obata, and M. Niwa, Mater. Trans. **56**, 1488 (2015).

[34] K. Özdoğan, E. Şaşıoğlu, and I. Galanakis, J. Appl. Phys. (Melville, NY) **113**, 193903 (2013).

[35] N. Zheng and Y. Jin, J. Magn. Magn. Mater. **324**, 3099 (2012).

[36] E. Vilanova Vidal, H. Schneider, and G. Jakob, Phys. Rev. B **83**, 174410 (2011).

[37] The asymmetric component is calculated as $MR(H) = [M(H) - M(-H)]/2$, while the symmetric component is calculated as $MR(H) = [M(H) + M(-H)]/2$.

[38] S. Agarwal, B. Wang, H. Yang, P. Dhanapal, Y. Shen, J. Wang, H. Wang, J. Zhao, and R.-W. Li, Phys. Rev. B **97**, 214427 (2018).

[39] N. Nagaosa, J. Sinova, S. Onoda, A. H. MacDonald, and N. P. Ong, Rev. Mod. Phys. **82**, 1539 (2010).

[40] M. Newwille, B. Ravel, D. Haskel, J. Rehr, E. Stern, and Y. Yacoby, Phys. B (Amsterdam) **208**, 154 (1995).

[41] J. Smit, Physica (Amsterdam) **24**, 39 (1958).

[42] R. Karplus and J. M. Luttinger, Phys. Rev. **95**, 1154 (1954).

[43] G. Sundaram and Q. Niu, Phys. Rev. B **59**, 14915 (1999).

[44] L. Berger, Phys. Rev. B **2**, 4559 (1970).

[45] Y. Tian, L. Ye, and X. Jin, Phys. Rev. Lett. **103**, 087206 (2009).

[46] C. Yu, T.-J. Zhu, R.-Z. Shi, Y. Zhang, X.-B. Zhao, and J. He, Acta Mater. **57**, 2757 (2009).

[47] K. Hayashi, M. Eguchi, and Y. Miyazaki, J. Electron. Mater. **46**, 2710 (2017).

[48] C. S. Lue and Y.-K. Kuo, Phys. Rev. B **66**, 085121 (2002).

[49] L. Huang, R. He, S. Chen, H. Zhang, K. Dahal, H. Zhou, H. Wang, Q. Zhang, and Z. Ren, Mater. Res. Bull. **70**, 773 (2015).

[50] C. Fu, Y. Liu, H. Xie, X. Liu, X. Zhao, G. J. Snyder, J. Xie, and T. Zhu, J. Appl. Phys. (Melville, NY) **114**, 134905 (2013).

[51] M. Sajjad, Q. Mahmood, N. Singh, and J. A. Larsson, ACS Appl. Energy Mater. **3**, 11293 (2020).

[52] S. Mukhopadhyay, D. S. Parker, B. C. Sales, A. A. Puretzky, M. A. McGuire, and L. Lindsay, Science **360**, 1455 (2018).

[53] XRD and EXAFS measurements reveal a DO_3-type disorder in CFVS, which in the present case arises due to disorder between Co and V sites as well as between Fe and V sites. To simulate the experimentally observed structure, a $2 \times 2 \times 2$ supercell of the primitive cell of the most stable ordered configuration (type I) of CFVS was constructed. This supercell contains a total of 32 atoms, including eight atoms of each kind. In a $2 \times 2 \times 2$ supercell, exchanging one of the eight Co or Fe atom positions with one of the eight V atom positions leads to a 12.5% swap disorder between Co or Fe atoms and V atoms. All possible configurations for replacement of Co or Fe atoms by V atoms and vice versa were simulated, and the results of the energetically most stable configurations were chosen to present here. As compared with the completely ordered structure, the atom projected local moments in the disordered case change considerably due to the change in the local atomic environment.